

# Unveiling Linker-Born Electron Spin Qubits in UiO-66-NH<sub>2</sub> MOF

Eugenio Ota<sup>1</sup>, Timur Biktagirov<sup>2</sup>, Leopold Trost<sup>3</sup>, Patrick Dörflinger<sup>4</sup>, Olga Trukhina<sup>4</sup>, Daniel Klose<sup>3</sup>, Wolf Gero Schmidt<sup>2</sup>, Anastasiia Kul'taeva<sup>4</sup>

<sup>1</sup>*Research Initiative for Supra Materials, Shinshu University, 4-17- Wakasato, Nagano city, 380-8553, Japan*

<sup>2</sup>*Physics Department, University of Paderborn, D-33098 Paderborn, Germany*

<sup>3</sup>*Institute of Molecular Physical Science, ETH Zurich, 8093 Zurich, Switzerland*

<sup>4</sup>*Experimental Physics 6 and Würzburg-Dresden Cluster of Excellence ct.qmat, Julius-Maximilian University of Würzburg, 97074 Würzburg, Germany*

**Abstract:** Metal-organic frameworks (MOFs), with their high porosity and large internal surface area, provide versatile platforms for integrating spin centers with potential applications in catalysis and quantum sensing. Here, we identify a stable NH• radical spin center in UiO-66-NH<sub>2</sub>, a zirconium-based MOF with aminoterephthalic acid (TPA-NH<sub>2</sub>) linkers. Using electron paramagnetic resonance spectroscopy and density functional theory calculations, we determine the nature and spin Hamiltonian parameters of this radical. We also demonstrate that the NH• spin center exhibits a relatively long coherence time, making it a strong candidate for quantum sensing. Since this spin center is intrinsic to TPA-NH<sub>2</sub> linkers, our findings open new directions for leveraging organic radicals in MOFs for quantum technologies beyond the UiO-66-NH<sub>2</sub> family.

## INTRODUCTION

Spin centers in solid-state materials have gained considerable interest for their potential in quantum technology applications, including qubits, quantum sensors, and single-photon emitters [1, 2]. One of the best-known examples is the nitrogen-vacancy (NV) center in diamond, which demonstrates excellent quantum coherence and versatility in quantum information processing and sensing [3]. The success of the NV center has spurred interest in exploring spin centers in other materials, such as silicon carbide (SiC) and hexagonal boron nitride (hBN) [4–6]. While conventional inorganic semiconductors have dominated as hosts for spin centers, the emergence of metal-organic frameworks (MOFs) introduces an exciting alternative.

MOFs are crystalline materials composed of metal ions coordinated to organic ligands, forming porous networks. Their high tunability and mature synthesis technology allow for precise, controllable spatial arrangement of spin centers [7–9]. Their high porosity and large inner surface area, which can host abundant spin centers accessible to guest molecules, make them particularly promising candidates for quantum sensing applications [10].

Historically, transition metal ions, which are integral to the MOF structure, have been considered the primary candidates for quantum sensors. For example, Cu<sup>2+</sup> ions in Zn-doped

HKUST-1 MOF have been shown to function as effective microwave-addressable quantum sensors, enabling the detection of guest molecules with atomic-scale resolution via magnetic resonance techniques [10, 11]. However, recent interest has shifted to incorporating and leveraging organic radicals as spin centers bound to MOF linkers, due to their long spin coherence times, straightforward synthesis, and tunable properties enabled by organic chemistry [12–14].

In this work, we identify a stable organic radical native to MOFs containing 2-aminoterephthalic acid (TPA-NH<sub>2</sub>) as a linker. Specifically, we focus on the UiO-66-NH<sub>2</sub> MOF [15], which is widely recognized for its exceptional chemical stability and compelling photocatalytic properties. The electron paramagnetic resonance (EPR) signal of this spin center is commonly observed in as-synthesized UiO-66-NH<sub>2</sub> [16] and as a result of free radical reactions [17]. However, the precise identification of this spin center has remained elusive. Using a combination of continuous-wave (CW) EPR and density functional theory (DFT) calculations, we show conclusively that this spin center is the TPA-NH• (aminoterephthalate) radical, likely formed through hydrogen atom abstraction from a fraction of the linker NH<sub>2</sub> groups during synthesis. Additionally, our advanced pulsed EPR measurements reveal that the NH• spin center exhibits long coherence times, allowing for nuclear spin readout and highlighting its potential as a microwave-addressable quantum sensor.

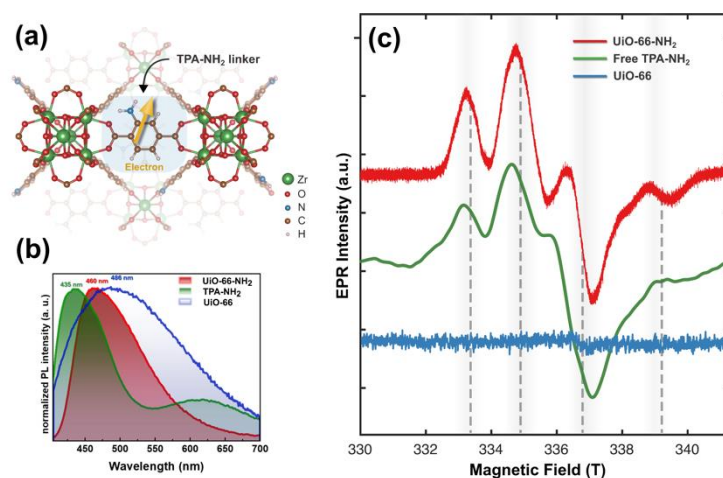


**Figure 1.** (a) Atomic structure of UiO-66-NH<sub>2</sub>, with the arrow schematically indicating an electron spin center as a quantum sensor point on the linker. (b) Room temperature steady-state photoluminescence emission spectra of UiO-66-NH<sub>2</sub> MOF, free TPA-NH<sub>2</sub> powder and UiO-66 MOF. (c) Comparison of room-temperature X-band CW EPR spectra of UiO-66-NH<sub>2</sub> MOF, free TPA-NH<sub>2</sub>, and UiO-66 MOF. The four-line splitting pattern associated with aminoterephthalate radicals is indicated with dotted lines.

## RESULTS AND DISCUSSION

The UiO-66-NH<sub>2</sub> powder sample was synthesized according to the procedure described in the Methods section (see Supporting Information). The metal nodes of this MOF consist of zirconium oxide clusters, specifically Zr<sub>6</sub>O<sub>4</sub>(OH)<sub>4</sub> units coordinated by the carboxylate groups of the TPA-NH<sub>2</sub> linkers (Figure 1a). Most of the TPA-NH<sub>2</sub> molecules used in the synthesis are incorporated in UiO-66-NH<sub>2</sub> as linkers, while the remaining are washed out from the porous structure. This is supported by Figure 1b that presents the comparison of the steady-state

photoluminescence (PL) emission spectra of the studied UiO-66-NH<sub>2</sub> sample, free TPA-NH<sub>2</sub> powder, and the sample of UiO-66 MOF that is formed of TPA without the NH<sub>2</sub> group. The observed shift to lower wavelengths in the emission peak between UiO-66 and UiO-66-NH<sub>2</sub> indicates that the MOF sample incorporates TPA-NH<sub>2</sub> as linkers, with only a negligible amount of free TPA-NH<sub>2</sub> in the structure. This conclusion is further supported by the absence of the 620 nm PL peak associated with the pristine TPA-NH<sub>2</sub> linker. It is important to note that modifications to the MOF can lead to changes in the electronic structure, which is reflected in the shift of the PL peak maxima [18]. The overall PL intensity of the UiO-66-NH<sub>2</sub> sample is higher than that of UiO-66, with a photoluminescence quantum yield of 2.4% compared to 1.5%. This increase in PL intensity may indicate improved charge transfer between the ligands and metal clusters [18, 19]. However, due to the complex nature of PL, other factors such as crystallinity, particle size, and the presence of defects, among others, may also contribute to this behavior [19, 20].

Next, in comparing the room-temperature CW EPR spectra of these samples (Figure 1c), we find that UiO-66-NH<sub>2</sub> and free TPA-NH<sub>2</sub> exhibit similar EPR spectra with an identical splitting pattern. At the same time, this EPR signature is absent in UiO-66. Therefore, we conclude that the observed spin center is intrinsic to aminoterephthalic acid, and not associated with the MOF metal nodes. Furthermore, the uniform saturation behavior upon increasing the microwave power observed for the four EPR lines (Supplementary Figure S2) suggests that the lines originate from a single type of spin center. Different types of spin centers would likely show varied saturation behaviors due to differences in their electron spin relaxation times. Therefore, the observed four-line pattern spectrum can be attributed to hyperfine (HF) interactions between an electron spin and nearby nuclear spins. Additionally, we found that the EPR spectral shape was not significantly affected by cooling to cryogenic temperatures (Supplementary Figure S3), indicating that the radical is rigidly anchored within the MOF and does not exhibit detectable rotational mobility.

Consequently, the measured EPR spectrum can be described using the conventional “solid-state” spin Hamiltonian:

$$\hat{H} = \mu_B B \cdot g \cdot \hat{S} + \sum_i \hat{S} \cdot A_i \cdot \hat{I}_i \quad (1)$$

where  $\hat{S}$  is the electron spin operator (with the eigenvalue  $S = 1/2$ ),  $g$  is  $g$ -tensor that reflects contributions from spin-orbit coupling to the free electron  $g$ -factor,  $B$  is the magnetic field vector,  $\mu_B$  is the Bohr magneton,  $A_i$  is the tensor of HF interaction with  $i$ -th nucleus and  $\hat{I}_i$  is the corresponding nuclear spin operator. The observed splitting between the four EPR lines ( $\sim 2$  mT) and their relative intensities suggest that the unpaired electron interacts with one <sup>14</sup>N (nuclear spin  $I = 1$ ) and one <sup>1</sup>H (nuclear spin  $I = 1/2$ ) nucleus with nearly equivalent effective HF coupling of about 60 MHz. We therefore provisionally assign the observed EPR spectra to a radical formed by hydrogen atom removal from the NH<sub>2</sub> moiety of the linker, resulting in the spin-bearing NH• group. Given that the hydrogen in NH<sub>2</sub> is acidic in nature, this reaction is favorable for various aniline derivatives and can proceed spontaneously, for example, due to free radical-assisted deprotonation [21–23].

To validate this assignment, we performed DFT modeling of the NH• radical in the structure of UiO-66-NH<sub>2</sub> and calculated principal values of its spin Hamiltonian parameters (see the Methods section in Supporting Information). The results reveal the appearance of localized defect states in the electronic structure of the radical-containing MOF (Figure 2a). First, the

NH• radical introduces a half-filled  $\pi$  type electronic state into the band gap of UiO-66-NH<sub>2</sub> in which the unpaired electron is in the p-orbital perpendicular to the plane of the linker. The highest fully occupied state of the radical is situated around 1 eV below the highest occupied states of the non-defective linkers (the formal valence band maximum) and features an electron residing in the  $sp^2$  orbital ( $\sigma_N$  type state). This agrees with the typical electronic structure of R-NH• radicals [24]. As a result, the electron-spin density of the radical is well-confined within the single defective MOF linker, primarily on the NH• group with delocalization over the aromatic moiety (Figure 2b).

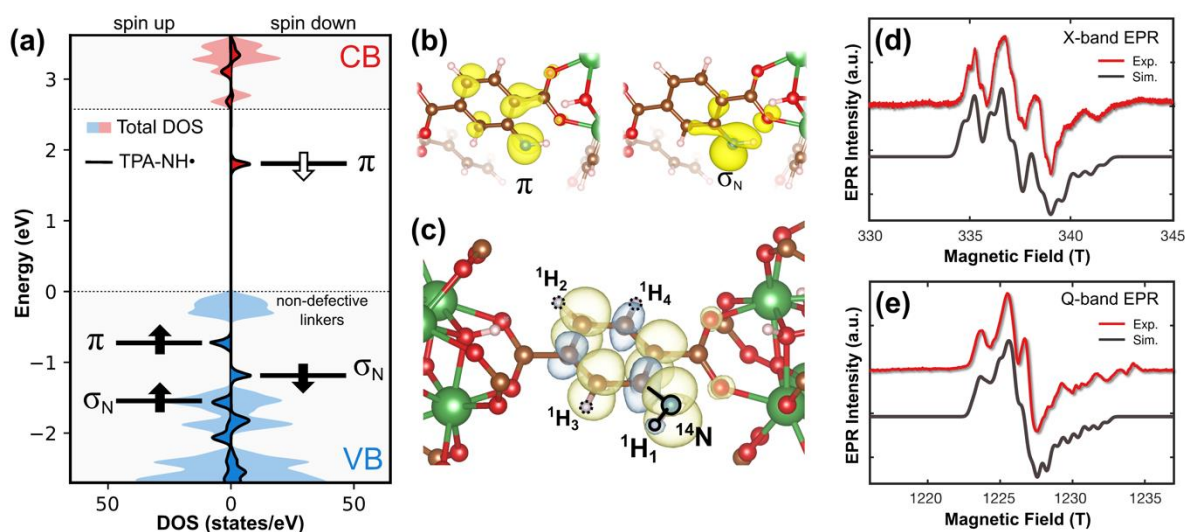


**Figure 2.** (a) DFT calculated total density of states (DOS; filled area; *blue*–occupied states, *red*–unoccupied states) and DOS projected onto the atoms of the radical-containing TPA-NH• linker in the UiO-66-NH<sub>2</sub> supercell (solid lines). Relevant Kohn-Sham states of the radical moiety are schematically shown with horizontal lines. Solid arrows depict occupied states, and an open arrow depicts an unoccupied state. (b) Charge density isosurfaces of the highest half-filled ( $\pi$ ) and fully occupied ( $\sigma_N$ ) orbitals of TPA-NH• in UiO-66-NH<sub>2</sub>. (c) Electron spin density distribution of the NH• radical in UiO-66-NH<sub>2</sub>. Yellow and blue lobes represent negative and positive isovalues, respectively; the isosurface absolute value is 0.002 e/Bohr<sup>3</sup>. (d) Simulation of the X-band and (e) Q-band EPR spectra of UiO-66-NH<sub>2</sub> based on the DFT-calculated spin Hamiltonian parameters (listed in Table S1).

The DFT-calculated spin Hamiltonian principal values are listed in Table S1, and the EPR spectrum simulation using these parameters is presented in Figure 2d,e and Figure S1. Here, we also include a spectrum acquired in Q-band (at ~34 GHz) [25], which, due to the higher magnetic field, provides enhanced resolution of  $g$ -factor anisotropy and allows a clear distinction between HF splitting and Zeeman contributions (cf. Eq. (1)). In agreement with our hypothesis, the <sup>14</sup>N and <sup>1</sup>H nuclei of the NH• group exhibit the largest principal values of the HF tensor, about 60 MHz, giving rise to the four-line pattern of the X-band spectrum and the overall shape of the Q-band spectrum. The HF interactions with the phenyl <sup>1</sup>H nuclei are unresolved within the linewidth but contribute to the line shape. In the simulation, the DFT-calculated principal values of the HF tensors were used as is, while their Euler rotation angles with respect to the  $g$ -tensor were optimized for a better fit with a maximum of 15° deviation from the DFT values (see Supplementary Table S1). The results signify that both the magnitude of HF couplings and the mutual orientation of their principal directions of the tensors fit both the X-band and Q-band experimental data, providing decisive evidence for the proposed nature of the radical.

Next, we explored the coherence properties of the identified spin center, using X-band pulsed EPR experiments measured at 50 K. The echo-detected field-sweep (EDFS) spectrum of UiO-66-NH<sub>2</sub>, obtained using the Hahn-echo pulse sequence is shown in Supplementary Figure S4. Its close similarity with the first integral form of the CW EPR spectrum indicates that all relevant transitions are excited by pulsed EPR, confirming that the same spin centers are probed in both types of experiments.

We determine the spin-coherence time  $T_2$  of the NH• spin center from the decay of the Hahn-echo magnitude as a function of the time delay  $\tau$  between microwave pulses (Figure 3a). The  $T_2$  time reflects how long the spin coherence is preserved before dephasing due to interactions with the surrounding nuclear spins and other spin centers. The data in Figure 3a were fit with a stretched exponential model of the form  $I(\tau) = \exp(-[\tau/T_2]^\beta)$ , revealing a  $T_2$  time of 1.129  $\mu\text{s}$  with a stretching parameter  $\beta = 0.91$ . This value of  $T_2$  is in the range observed for high-density spin defects in diamond [26], SiC [27, 28], and hBN [29]. The stretching parameter indicates the disorder in the electron spin ensemble resulting in a distribution of coherence times and depends on the microscopic nature of spin-flip dynamics that drives the decoherence process depending on the surrounding spin-bath [30–32].

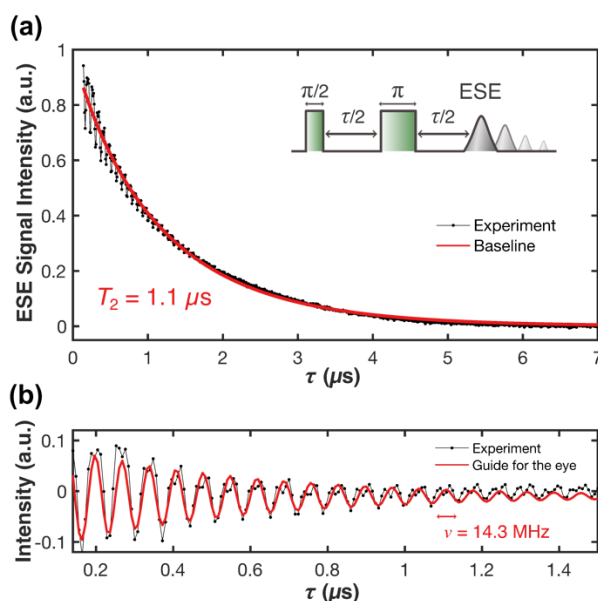


**Figure 3.** (a) Hahn-echo decay (black) of the NH• spin center measured as a function of the time delay  $\tau$  between the microwave pulses. The applied microwave pulse sequence is shown in the inset. A stretched exponential fit (red line) reveals a decay time  $T_2 = 1.129 \mu\text{s}$ . (b) Modulations of the decay curve after subtracting the baseline.

Generally, the  $T_2$  time is known to be inversely proportional to the concentration of nuclear spins [33]. Therefore, understanding the nuclear spin environment of the NH• spin (beyond the nearest nuclei already explored by CW EPR and DFT) can help rationalize and optimize its coherence properties. Insights about coherent coupling to the nuclear spin bath can be gleaned from the analysis of the oscillatory behavior of the Hahn-echo decay seen in Figure 3a and even more prominently in Figure 3b after subtracting the stretched exponential contribution. This effect, known as electron spin echo envelope modulation, ESEEM [34]. The modulation depth reflects the number and distribution of nuclei interacting with the

$\text{NH}\bullet$  electron spin [35]. The modulation frequency is defined by the nuclear resonance frequencies of the coupled nuclear magnetic moments [36]. The nuclear modulation pattern in Figure 3b is dominated by an oscillation frequency close to the Larmor frequency of  $^1\text{H}$  ( $\nu_L^H \approx 14.3$  MHz at the experimental magnetic field).

To gather more details about the nuclei that contribute to the observed modulations, we performed a 3-pulse ESEEM experiment using the pulse sequence shown in Figure 4a. In this sequence, the second pulse transfers electron coherence into nuclear coherence, which evolves and decays with mainly the transverse nuclear relaxation time until the third pulse transfers it back to the electron spin [36]. Therefore, the envelope decay is defined predominantly by nuclear relaxation, which is substantially longer compared to the electron  $T_2$  time governing the envelope decay in the Hahn-echo experiment, thus enabling a significantly better spectral resolution. The set of three-pulse envelopes depicted in Figure 4b was recorded at different intervals  $\tau$  between the first two microwave pulses, allowing us to suppress “blind spot” artifacts and achieve better resolution in the Fourier-transform magnitude spectrum (Fig. 4c). Accordingly, the 3-pulse ESEEM magnitude shown in Figure 4d is an average over these six envelopes.

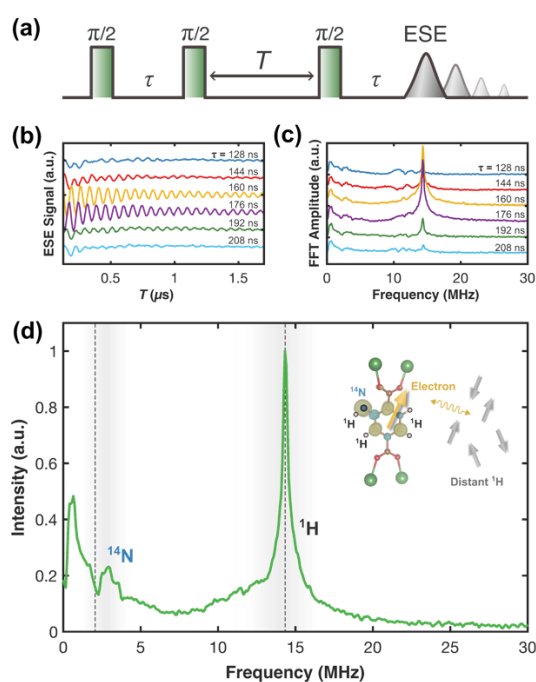


Figure 4. (a) 3-pulse ESEEM pulse sequence and (b) time traces measured at 6 different  $\tau$ -values (top to bottom: 128 ns, 144 ns, 160 ns, 176 ns, 192 ns, and 208 ns). (c) Fourier-transformed magnitude spectra of the 3-pulse ESEEM data with Hamming window and cross-term averaging (sum of 6 different  $\tau$ ). (d) ESEEM sum spectrum; hydrogen transitions are dominant and found at the corresponding Larmor frequency (14.3 MHz, labeled as  $^1\text{H}$ ). A peak assigned to  $^{14}\text{N}$  double quantum transitions showing the HF coupling is marked as  $^{14}\text{N}$ , and the corresponding Larmor frequency ( $2 \times 1.03$  MHz) is indicated with a dotted line.

The most prominent feature of the Fourier-transform ESEEM spectrum is a signal centered around  $\nu_L^H$ , associated with hyperfine-coupled  $^1\text{H}$  nuclear spins. Each nuclear spin contributes to the ESEEM spectrum at both sides of the corresponding Larmor frequency with the shift defined by its individual HF coupling tensor [36]. Since the magnitude of the dipolar

contributions to the HF interaction depends on the distance between the electron and nuclear spins, broad shoulders around  $\nu_L^H$  are caused primarily by the  $^1\text{H}$  atoms located in the MOF structure near the  $\text{NH}\bullet$  group [10]. At the same time, the sharp peak at  $\nu_L^H$  signifies that the  $^1\text{H}$  nuclear spin ensemble coupled to the electron spin of  $\text{NH}\bullet$  is dominated by the distribution of distant nuclei, which we associate with solvent molecules distributed in the pore system of UiO-66- $\text{NH}_2$ . Additionally, a much weaker signal observed in Figure 4d near twice the Larmor frequency of  $^{14}\text{N}$  that is assigned to  $^{14}\text{N}$  double quantum transitions and shows the presence of the hyperfine-coupled  $^{14}\text{N}$  [37].

The results indicate that the  $\text{NH}\bullet$  spin center is immersed in a nuclear spin bath comprising not only the  $^{14}\text{N}$  and  $^1\text{H}$  nuclei of the radical, but also of the more distant  $^1\text{H}$  nuclei of solvent molecules distributed in the pores. Therefore, while the measured microsecond-range coherence  $T_2$  time is already remarkably long, further manipulation involving the removal of solvent from pores through MOF activation can extend  $T_2$  by reducing decoherence pathways.

It should be noted that while the  $T_2$  coherence time in solids driven by nuclear spin diffusion doesn't usually exhibit a pronounced temperature dependence, overall spin coherence at ambient conditions (room temperature) is often limited by the spin-lattice relaxation time,  $T_1$  [38]. The dominant effect that determines the  $T_1$  time is the coupling between the electron spin and the lattice vibrational modes. While we plan a detailed investigation of the thermal behavior of the  $T_1$  time in future works, here we study the spin-lattice relaxation at 50 K using the inversion recovery pulse sequence (see Supplementary Figure S4). We obtained a compelling  $T_1$  of almost one millisecond ( $T_1 = 956 \mu\text{s}$ ), indicating that the  $\text{NH}\bullet$  spin center enables efficient coherence operations, at cryogenic temperatures.

## OUTLOOK

In conclusion, we identified a native radical defect commonly observed in UiO-66- $\text{NH}_2$ , a MOF material with a broad range of established technological applications and remarkable physicochemical properties. This  $\text{NH}\bullet$  radical is likely formed by hydrogen atom abstraction from the  $\text{NH}_2$  group of the organic linker during synthesis. Through a combination of EPR spectroscopy and DFT calculations, we elucidated its atomic and electronic structure, spin density localization, and spin Hamiltonian parameters. The compelling spin coherence time  $T_2 > 1 \mu\text{s}$ , along with the observed electron-nuclear coherent coupling effects, suggests that the spin center can potentially operate as a microwave-addressable quantum sensor. Unlike radicals introduced through post-synthetic modifications, this radical forms as an inherent part of the MOF structure, potentially enhancing stability and coherence due to its integration within the framework. Given that this spin center is intrinsic to the linker, distributed within a three-dimensional network, and easily accessed through the MOF's porous structure, our findings open new avenues for designing highly sensitive quantum sensors based on MOFs that extend beyond the UiO-66- $\text{NH}_2$  family.

## SUPPORTING INFORMATION

Full experimental and computational details and additional spectroscopic data (PDF)

## ACKNOWLEDGEMENTS

The authors thank Professor Vladimir Dyakonov for fruitful discussion. DK gratefully acknowledges financial support from ETH research grant ETH-35221. TB and WGS acknowledge the Paderborn Center for Parallel Computing (PC2) for the provided computational resources. AK acknowledges financial support from the Würzburg-Dresden Cluster of Excellence on Complexity and Topology in Quantum Matter ct.qmat (EXC 2147, DFG project ID 390858490). P.D. acknowledges the German Research Foundation (DFG) program SPP2196 under DY18/14-2 (Project number 424101351).

## REFERENCES

1. Wolfowicz, G.; Heremans, F. J.; Anderson, C.; Kanai, S.; Seo, H.; Gali, A.; Galli, G.; Awschalom, D. D. Quantum Guidelines for Solid-State Spin Defects. *Nat. Rev. Mater.* **2021**, *6* (10), 906–925. DOI: 10.1038/s41578-021-00306-y.
2. Weber, J. R.; Koehl, W. F.; Varley, J. B.; Janotti, A.; Buckley, B. B.; Van de Walle, C. G.; Awschalom, D. D. Quantum Computing with Defects. *Proc. Natl. Acad. Sci. U.S.A.* **2010**, *107* (19), 8513–8518. DOI: 10.1073/pnas.1003052107.
3. Doherty, M. W.; Manson, N. B.; Delaney, P.; Jelezko, F.; Wrachtrup, J.; Hollenberg, L. C. L. The Nitrogen-Vacancy Colour Centre in Diamond. *Phys. Rep.* **2013**, *528* (1), 1–45. DOI: 10.1016/j.physrep.2013.02.001.
4. von Bardeleben, H. J.; Cantin, J.-L.; Gerstmann, U.; Schmidt, W. G.; Biktagirov, T. Spin Polarization, Electron–Phonon Coupling, and Zero-Phonon Line of the NV Center in 3C-SiC. *Nano Lett.* **2021**, *21* (19), 8119–8125. DOI: 10.1021/acs.nanolett.1c02564.
5. Kraus, H.; Soltamov, V. A.; Fuchs, F.; Simin, D.; Sperlich, A.; Baranov, P. G.; Astakhov, G. V.; Dyakonov, V. Magnetic Field and Temperature Sensing with Atomic-Scale Spin Defects in Silicon Carbide. *Sci. Rep.* **2014**, *4*, 5303. DOI: 10.1038/srep05303.
6. Gottscholl, A.; Kianinia, M.; Soltamov, V.; Orlinskii, S.; Mamin, G.; Bradac, C.; Kasper, C.; Krambrock, K.; Sperlich, A.; Toth, M.; Aharonovich, I.; Dyakonov, V. Initialization and Read-Out of Intrinsic Spin Defects in a van der Waals Crystal at Room Temperature. *Nat. Mater.* **2020**, *19* (5), 540–545. DOI: 10.1038/s41563-020-0619-6.
7. Yamabayashi, T.; Atzori, M.; Tesi, L.; Cosquer, G.; Santanni, F.; Boulon, M.-E.; Morra, E.; Benci, S.; Torre, R.; Chiesa, M.; Sorace, L.; Sessoli, R.; Yamashita, M. Scaling Up Electronic Spin Qubits into a Three-Dimensional Metal–Organic Framework. *J. Am. Chem. Soc.* **2018**, *140* (38), 12090–12101. DOI: 10.1021/jacs.8b06733.
8. Yu, C.-J.; Krzyaniak, M. D.; Fataftah, M. S.; Wasielewski, M. R.; Freedman, D. E. A Concentrated Array of Copper Porphyrin Candidate Qubits. *Chem. Sci.* **2019**, *10* (6), 1702–1708. DOI: 10.1039/C8SC04435J.
9. Zadrozny, J. M.; Gallagher, A. T.; Harris, T. D.; Freedman, D. E. A Porous Array of Clock Qubits. *J. Am. Chem. Soc.* **2017**, *139* (20), 7089–7094. DOI: 10.1021/jacs.7b03123.
10. Kultaeva, A.; Pöppel, A.; Biktagirov, T. Atomic-Scale Quantum Sensing of Ensembles of Guest Molecules in a Metal–Organic Framework with Intrinsic Electron Spin Centers. *J. Phys. Chem. Lett.* **2022**, *13* (29), 6737–6742. DOI: 10.1021/acs.jpcllett.2c01429.



11. Kultaeva, A.; Böhlmann, W.; Hartmann, M.; Biktagirov, T.; Pöppel, A. Adsorption of Olefins at Cupric Ions in Metal–Organic Framework HKUST-1 Explored by Hyperfine Spectroscopy. *J. Phys. Chem. Lett.* **2019**, *10* (24), 7488–7493. DOI: 10.1021/acs.jpcclett.9b02952.
12. Oanta, A. K.; Collins, K. A.; Evans, A. M.; Pratik, S. M.; Hall, L. A.; Strauss, M. J.; Marder, S. R.; D'Alessandro, D. M.; Rajh, T.; Freedman, D. E.; Li, H.; Brédas, J.-L.; Sun, L.; Dichtel, W. R. Electronic Spin Qubit Candidates Arrayed within Layered Two-Dimensional Polymers. *J. Am. Chem. Soc.* **2023**, *145* (1), 689–696. DOI: 10.1021/jacs.2c11784.
13. Sun, L.; Yang, L.; Dou, J.-H.; Li, J.; Skorupskii, G.; Mardini, M.; Tan, K. O.; Chen, T.; Sun, C.; Oppenheim, J. J.; Griffin, R. G.; Dincă, M.; Rajh, T. Room-Temperature Quantitative Quantum Sensing of Lithium Ions with a Radical-Embedded Metal–Organic Framework. *J. Am. Chem. Soc.* **2022**, *144* (41), 19008–19016. DOI: 10.1021/jacs.2c07692.
14. Jellen, M. J.; Ayodele, M. J.; Cantu, A.; Forbes, M. D. E.; Garcia-Garibay, M. A. 2D Arrays of Organic Qubit Candidates Embedded into a Pillared-Paddlewheel Metal–Organic Framework. *J. Am. Chem. Soc.* **2020**, *142* (43), 18513–18521. DOI: 10.1021/jacs.0c07251.
15. Cavka, J. H.; Jakobsen, S.; Olsbye, U.; Guillou, N.; Lamberti, C.; Bordiga, S.; Lillerud, K. P. A New Zirconium Inorganic Building Brick Forming Metal Organic Frameworks with Exceptional Stability. *J. Am. Chem. Soc.* **2008**, *130* (42), 13850–13851. DOI: 10.1021/ja8057953.
16. Long, J.; Wang, S.; Ding, Z.; Wang, S.; Zhou, Y.; Huang, L.; Wang, X. Amine-Functionalized Zirconium Metal–Organic Framework as Efficient Visible-Light Photocatalyst for Aerobic Organic Transformations. *Chem. Commun.* **2012**, *48* (95), 11656–11658. DOI: 10.1039/C2CC34620F.
17. Ibrahim, A. H.; Haikal, R. R.; Eldin, R. S.; El-Mehalmey, W. A.; Alkordi, M. H. The Role of Free-Radical Pathway in Catalytic Dye Degradation by Hydrogen Peroxide on the Zr-Based UiO-66-NH<sub>2</sub> MOF. *ChemistrySelect* **2021**, *6* (42), 11892–11897. DOI: 10.1002/slct.202102955.
18. Rosales-Martínez, C.; Assis, M.; Castillo-Blas, C.; Abánades Lázaro, I. Tuning the Electronic Properties of Zr UiO-66 through Defect-Functionalised Multivariate Modulation. *Chem. Commun.* **2024**, *60* (63), 8280–8283. DOI: 10.1039/D4CC02581D.
19. Alvaro, M.; Carbonell, E.; Ferrer, B.; Llabrés i Xamena, F. X.; Garcia, H. Semiconductor Behavior of a Metal-Organic Framework (MOF). *Chem. Eur. J.* **2007**, *13* (18), 5106–5112. DOI: 10.1002/chem.200601003.
20. Fu, Y.; Wu, J.; Du, R.; Guo, K.; Ma, R.; Zhanga, F.; Zhu, W.; Fan, M. Temperature Modulation of Defects in NH<sub>2</sub>-UiO-66(Zr) for Photocatalytic CO<sub>2</sub> Reduction. *RSC Adv.* **2019**, *9*, 37733–37738. DOI: 10.1039/C9RA08097J.
21. Singh, T. S.; Gejji, S. P.; Rao, B. S. M.; Mohan, H.; Mittal, J. P. Radiation Chemical Oxidation of Aniline Derivatives. *J. Chem. Soc., Perkin Trans. 2* **2001**, *7*, 1205–1211. DOI: 10.1039/B009020O.

22. Lin, S.-Y.; Chou, S.-L.; Tseng, C.-M.; Wu, Y.-J. IR Absorption Spectra of Aniline Cation, Anilino Radical, and Phenylnitrene Isolated in Solid Argon. *Spectrochim. Acta, Part A* **2022**, *276*, 121233. DOI: 10.1016/j.saa.2022.121233.
23. Francisco-Márquez, M.; Aguilar-Fernández, M.; Galano, A. Anthranilic Acid as a Secondary Antioxidant: Implications to the Inhibition of  $\cdot\text{OH}$  Production and the Associated Oxidative Stress. *Comput. Theor. Chem.* **2016**, *1077*, 18–24. DOI: 10.1016/j.comptc.2015.09.025.
24. Koenig, T.; Hoobler, J. A.; Klopfenstein, C. E.; Hedden, G.; Sunderman, F.; Russell, B. R. Electronic Configurations of Amido Radicals. *J. Am. Chem. Soc.* **1974**, *96* (14), 4573–4577. DOI: 10.1021/ja00821a036.
25. Fischer, J. W. A.; Stropp, J.; Tschaggelar, R.; Oberhänsli, O.; Alaniva, N.; Inoue, M.; Mashima, K.; Barnes, A. B.; Jeschke, G.; Klose, D. Design and Performance of an Oversized-Sample 35 GHz EPR Resonator with an Elevated Q Value. *Magn. Reson.* **2024**, *5* (2), 143–152. DOI: 10.5194/mr-5-143-2024.
26. Jelezko, F.; Gaebel, T.; Popa, I.; Gruber, A.; Wrachtrup, J. Observation of Coherent Oscillations in a Single Electron Spin. *Phys. Rev. Lett.* **2004**, *92* (7), 076401. DOI: 10.1103/PhysRevLett.92.076401.
27. Yang, L.-P.; Burk, C.; Widmann, M.; Lee, S.-Y.; Wrachtrup, J.; Zhao, N. Electron Spin Decoherence in Silicon Carbide Nuclear Spin Bath. *Phys. Rev. B* **2014**, *90* (24), 241203(R). DOI: 10.1103/PhysRevB.90.241203.
28. Soltamov, V. A.; Yavkin, B. V.; Anisimov, A. N.; Singh, H.; Bundakova, A. P.; Mamin, G. V.; Orlinskii, S. B.; Mokhov, E. N.; Suter, D.; Baranov, P. G. Relaxation Processes and High-Field Coherent Spin Manipulation in Color Center Ensembles in 6H-SiC. *Phys. Rev. B* **2021**, *103*, 195201. DOI: 10.1103/PhysRevB.103.195201.
29. Gottscholl, A.; Diez, M.; Soltamov, V.; Kasper, C.; Sperlich, A.; Kianinia, M.; Bradac, C.; Aharonovich, I.; Dyakonov, V. Room Temperature Coherent Control of Spin Defects in Hexagonal Boron Nitride. *Sci. Adv.* **2021**, *7* (14), eabf3630. DOI: 10.1126/sciadv.abf3630.
30. Davis, E. J.; Ye, B.; Machado, F.; Meynell, S. A.; Wu, W.; Mittiga, T.; Schenken, W.; Joos, M.; Kobrin, B.; Lyu, Y.; Wang, Z.; Bluvstein, D.; Choi, S.; Zu, C.; Bleszynski Jayich, A. C.; Yao, N. Y. Probing Many-Body Dynamics in a Two-Dimensional Dipolar Spin Ensemble. *Nat. Phys.* **2023**, *19*, 836–844. DOI: 10.1038/s41567-023-01944-5.
31. Mims, W. B. Phase Memory in Electron Spin Echoes, Lattice Relaxation Effects in  $\text{CaWO}_4$ : Er, Ce, Mn. *Phys. Rev.* **1968**, *168*, 370. DOI: 10.1103/PhysRev.168.370.
32. Jeschke, G. Nuclear Pair Electron Spin Echo Envelope Modulation. *J. Magn. Reson. Open* **2023**, *14*, 100094. DOI: 10.1016/j.jmro.2023.100094.
33. Widmann, M.; Lee, S.-Y.; Rendler, T.; Son, N. T.; Fedder, H.; Paik, S.; Yang, L.-P.; Zhao, N.; Yang, S.; Booker, I.; Denisenko, A.; Jamali, M.; Momenzadeh, S. A.; Gerhardt, I.; Ohshima, T.; Gali, A.; Janzén, E.; Wrachtrup, J. Coherent Control of Single Spins in Silicon Carbide at Room Temperature. *Nat. Mater.* **2015**, *14*, 164–168. DOI: 10.1038/nmat4145.

34. Dikanov, S. A.; Tsvetkov, Y. D. *Electron Spin Echo Envelope Modulation (ESEEM) Spectroscopy*; CRC Press, 1992.
35. Kevan, L.; Bowman, M. K.; Narayana, P. A.; Boeckman, R. K.; Yudanov, V. F.; Tsvetkov, Y. D. Electron Spin Echo Envelope Modulation of Trapped Radicals in Disordered Glassy Systems: Application to the Molecular Structure around Excess Electrons in  $\gamma$ -Irradiated 2-Methyltetrahydrofuran Glass. *J. Chem. Phys.* **1975**, *63* (1), 409–416. DOI: 10.1063/1.431119.
36. Schweiger, A. Pulsed Electron Spin Resonance Spectroscopy: Basic Principles, Techniques, and Examples of Applications. *Angew. Chem. Int. Ed. Engl.* **1991**, *30* (3), 265–292. DOI: 10.1002/anie.199102651.
37. Van Doorslaer, S.; Goldfarb, D.; Stoll, S. Hyperfine Spectroscopy-ESEEM. In *EPR Spectroscopy: Fundamentals and Methods*; Wiley: 2018; pp 377–400.
38. Yu, C.-J.; Krzyaniak, M. D.; Fataftah, M. S.; Wasielewski, M. R.; Freedman, D. E. A Concentrated Array of Copper Porphyrin Candidate Qubits. *Chem. Sci.* **2019**, *10*, 1702–1708. DOI: 10.1039/C8SC04435J.

## **SUPPORTING INFORMATION for**

### **Unveiling Linker-Born Electron Spin Qubits in UiO-66-NH<sub>2</sub> MOF**

Eugenio Otal<sup>1</sup>, Timur Biktagirov<sup>2</sup>, Leopold Trost<sup>3</sup>, Patrick Dörflinger<sup>4</sup>, Olga Trukhina<sup>4</sup>, Daniel Klose<sup>3</sup>, Wolf Gero Schmidt<sup>2</sup>, Anastasiia Kul'taeva<sup>4</sup>

#### **TABLE OF CONTENTS**

<b>Full experimental and computational details</b>	<b>S2</b>
<b>Table S1</b>   DFT calculated and fitted spin Hamiltonian parameters of TPA-NH•	<b>S4</b>
<b>Figure S1</b>   Simulation of X- and Q-band spectra using only two nearest and all nuclei	<b>S5</b>
<b>Figure S2</b>   Saturation behavior of the CW EPR spectrum of UiO-66-NH <sub>2</sub>	<b>S5</b>
<b>Figure S3</b>   Temperature dependence of the CW EPR spectrum of UiO-66-NH <sub>2</sub>	<b>S6</b>
<b>Figure S4</b>   X-band echo-detected field-sweep spectrum of UiO-66-NH <sub>2</sub>	<b>S6</b>
<b>Figure S5</b>   Determination of spin-lattice relaxation time of TPA-NH•	<b>S7</b>
<b>References</b>	<b>S7</b>

## FULL EXPERIMENTAL AND COMPUTATIONAL DETAILS

### Sample preparation

UiO-66-NH<sub>2</sub> was synthesized using a modified procedure previously reported by Katz et al. [1]. In a 500 ml Schott Duran flask, 300 ml of DMF and 20 ml of concentrated HCl were mixed under a fume hood. To this solution, 2.51 g of ZrCl<sub>4</sub> was added in small portions, also under the fume hood. The solid dissolved quickly, and then 2.68 g of 2-aminoterephthalic (BDC-NH<sub>2</sub>) acid was added to the resultant solution. To facilitate the dissolution of BDC-NH<sub>2</sub>, the mixture was subjected to an ultrasonic bath for 30 minutes. After complete dissolution, the screw-cap bottles were sealed and maintained at 120°C for 12 hours. The solids were isolated by centrifugation and washed twice with DMF and CH<sub>2</sub>Cl<sub>2</sub>.

### Continuous wave electron paramagnetic resonance (CW EPR) spectroscopy

The X-band CW EPR spectra (9.42 GHz) were measured on a commercial Magnettech spectrometer equipped with an Oxford ESR 900 He flow cryostat. A microwave power of 1 mW was chosen for optimal signal-to-noise ratio of the main EPR spectra without saturation effects. Experiments on the saturation behavior and temperature dependence of the EPR spectrum have also been conducted (see Figure S2 and Figure S3). A modulation amplitude of the external magnetic field of 2 Gauss was used to resolve the hyperfine EPR lines.

EPR spectra in Q-band were recorded on an Elexsys E580 EPR spectrometer equipped with a cryogen-free variable temperature cryostat (Cryogenic Ltd., London, UK) and a home-built dedicated CW EPR resonator for oversized sample tubes [2]. Data were acquired using 1001 points over a width of 50 mT, 0.005 mW microwave power to ensure non-saturating conditions, a lock-in conversion time 160.0 ms and a time constant 40.96 ms, a magnetic field modulation amplitude 0.05 mT and a modulation frequency 100 kHz, 240 scans were accumulated.

### Pulsed EPR spectroscopy

Pulsed X-band EPR experiments were performed on an Elexsys E680 EPR spectrometer (Bruker) with a dielectric ring resonator (MD-5, Bruker), a 1 kW TWT amplifier (Applied Systems Engineering Inc., Texas, USA) and a Helium flow EPR cryostat (CF935, Oxford Instruments) to maintain the temperature at 50 K.

The echo-detected EPR spectrum was measured using the Hahn echo sequence,  $\pi/2 - \tau - \pi - \tau$  - echo, with an interpulse delay  $\tau$  of 200 ns, 16/32 ns rectangular pulses for  $\pi/2$  and  $\pi$ , respectively. The echo was integrated with a boxcar integration window of 200 ns. Data were acquired by stepping the magnetic field over 50 mT in 501 points, using 100 shots per points with a shot repetition time of 8 ms and 10 scans were accumulated. 2pESEEM data were acquired by using the same sequence at the magnetic field corresponding to the maximum of the absorption spectrum and stepping the interpulse delay  $\tau$  in 1024 steps of 8 ns from 140 ns using a two-step phase cycle (+x - x) on the  $\pi/2$ -pulse with a boxcar echo integration

window of 32 ns, 10 shots per points and a shot repetition time of 2.6 ms, while 240 scans were accumulated.

3pESEEM data were acquired using the pulse sequence,  $\pi/2 - \tau - \pi/2 - T - \pi/2 - \tau - \text{echo}$ . Data were acquired for six different  $\tau$ -values by using the same sequence at the magnetic field corresponding to the maximum of the absorption spectrum and stepping the interpulse delay  $T$  in 512 steps of 8 ns from 128 ns using a four-step phase cycle with a boxcar echo integration window of 32 ns, 10 shots per points and a shot repetition time of 3 ms, while 420 scans were accumulated.

The longitudinal relaxation time,  $T_1$ , was measured using the inversion recovery sequence,  $\pi - t - \pi/2 - \tau - \pi - \tau - \text{echo}$ , with an interpulse delay  $\tau$  of 200 ns, 16/32 ns rectangular pulses for  $\pi/2$  and  $\pi$ , respectively, with a two-step phase cycle (+x - x) on the  $\pi/2$ -pulse to cancel out receiver offsets. The echo was integrated with a boxcar integration window of 32 ns. Data were acquired by stepping  $t$  from 1.2  $\mu\text{s}$  in steps of 20  $\mu\text{s}$  for 2048 points, using 4 shots per point with a shot repetition time of 53 ms and 9 scans were accumulated.

## Computational methods

DFT calculations of spin Hamiltonian parameters were performed with the ORCA (v. 6.0) program package [3] using the PBE exchange-correlation functional [4] and the def2-TZVP basis set [5]. The cluster model used in the calculations was cut from the crystal structure of UiO-66. It consisted of one linker and two SBUs with the remaining (unsaturated) coordination sites of the SBUs terminated by  $\text{HCOO}^-$  anions. During geometry optimization, the coordinates of the carbon atoms of each  $\text{HCOO}^-$  were fixed. To address the electronic structure of the radical-containing  $\text{NH}_2$ -UiO-66, a 126-atom MOF supercell with one spin center was modeled with the Quantum ESPRESSO package [6, 7] under periodic boundary conditions. The calculations used the hybrid HSE06 functional [8, 9], projector augmented wave pseudopotentials [10], 50 Ry kinetic energy cutoff, and  $\Gamma$ -point Brillouin zone sampling.

The simulations of the powder EPR spectra were carried out using the Matlab toolbox EasySpin [11]. The simulations were based on the spin Hamiltonian defined in Eq. (1) that included the anisotropic Zeeman interaction, and the anisotropic HF interactions between the electron spin and the  $^{14}\text{N}$  nuclear spin, as well as to the four  $^1\text{H}$  nuclear spins of the radical-containing linker of  $\text{NH}_2$ -UiO-66. The DFT-calculated spin Hamiltonian parameters were used as a starting point for EPR spectra simulations. During the simulations, the principal values of the  $g$ -tensor and the Euler rotation angles of the HF tensors were adjusted to obtain the best fit. The fitted spin Hamiltonian parameters are provided in Table S1.

## Photoluminescence

For the steady-state photoluminescence (SSPL) measurements an Edinburgh Instrument FLS 980 was used. The powder sample was measured in a reflection geometry and the emission of the sample was collimated. In front of the monochromator and the photomultiplier tube a 400 nm longpass filter was positioned, which blocks wavelengths below 400 nm. To measure the steady-state PL spectra, the samples were excited with a 375 nm laser having a spot size

of 100  $\mu\text{m}$  in diameter, a fluence of approximately 88  $\text{nj}/\text{cm}^2$ , and a repetition rate of 50 ns. For the PLQY measurements, an integrating sphere in an Edinburgh Instruments FLS 980 was used. The sample was excited with a 406 nm CW laser diode with 31.9  $\text{mW}/\text{cm}^2$ . The spot size was 0.03  $\text{cm}^2$  [12].

## ADDITIONAL DATA

**Table S1.** DFT calculated spin Hamiltonian parameters of TPA-NH• in UIO-66-NH<sub>2</sub> along with the parameters used to simulate the experimental X-band and Q-band EPR spectra in Fig. 2d,e. Simulation parameters are only explicitly given in the table if they were varied to fit the experimental spectra - otherwise the DFT values were used and kept fixed in the simulations.

		Principal Values*	Euler Rotation Angles to the $g$ -tensor**
$g$ -tensor	DFT	2.0026, 2.0032, 2.0053	
	Sim	2.0027, 2.0062, 2.0092	
<sup>14</sup> N HFI	DFT	59.59, -14.17, -13.39	-146.7, 10.2, 121.3
	Sim	<i>fixed</i>	-143.2, 9.2, 123.95
<sup>1</sup> H <sub>1</sub> HFI	DFT	-35.36, -58.13, 2.27	-108.1, 33.3, 81.0
	Sim	<i>fixed</i>	-108.5, 33.3, 80.4
<sup>1</sup> H <sub>2</sub> HFI	DFT	-17.11, -27.53, -6.20	93.1, 37.8, -99.3
	Sim	<i>fixed</i>	91.1, 39.9, -100.0
<sup>1</sup> H <sub>3</sub> HFI	DFT	-16.10, -20.84, -5.31	-78.5, 32.8, 78.3
	Sim	<i>fixed</i>	-72.7, 41.5, 69.7
<sup>1</sup> H <sub>4</sub> HFI	DFT	1.30, 5.64, 4.21	-108.0, 18.4, 101.9
	Sim	<i>fixed</i>	<i>fixed</i>

\*Principal values of the hyperfine tensors are in MHz

\*\*Euler rotation angles are in degrees

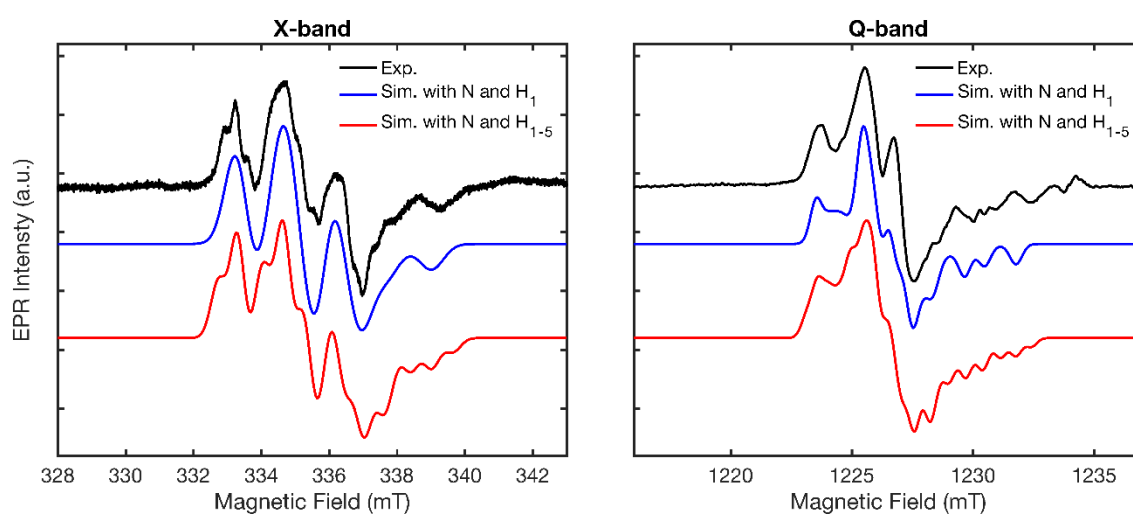


**Figure S1.** X-band (left) and Q-band (right) simulations of CW EPR spectra with the parameters listed in Table S1, including the contributions of only the two nuclei of the NH• group (<sup>14</sup>N and <sup>1</sup>H<sub>1</sub>; *blue line*) and all nuclei of the TPA-NH• linker (*red line*).

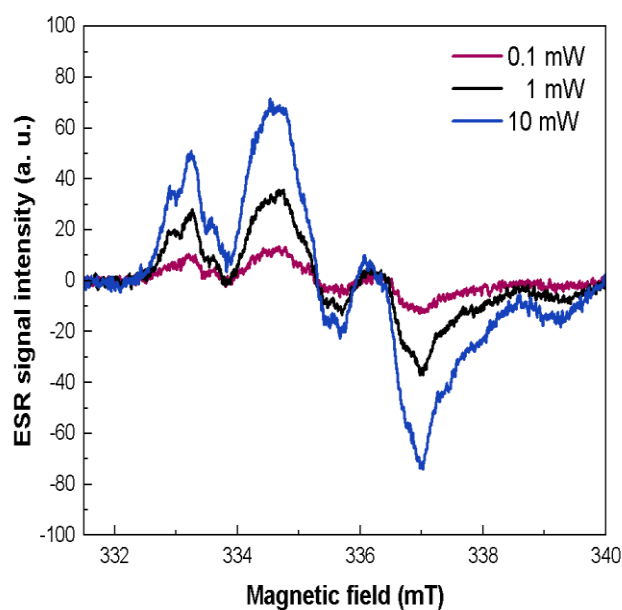


**Figure S2.** Saturation behavior of the CW EPR spectrum of UiO-66-NH<sub>2</sub>. The microwave power saturation experiment demonstrates a simultaneous increase in the EPR lines, which confirms the absence of superposition of lines with different nature (relaxation times and coordination geometry). The measurements were performed at room temperature.

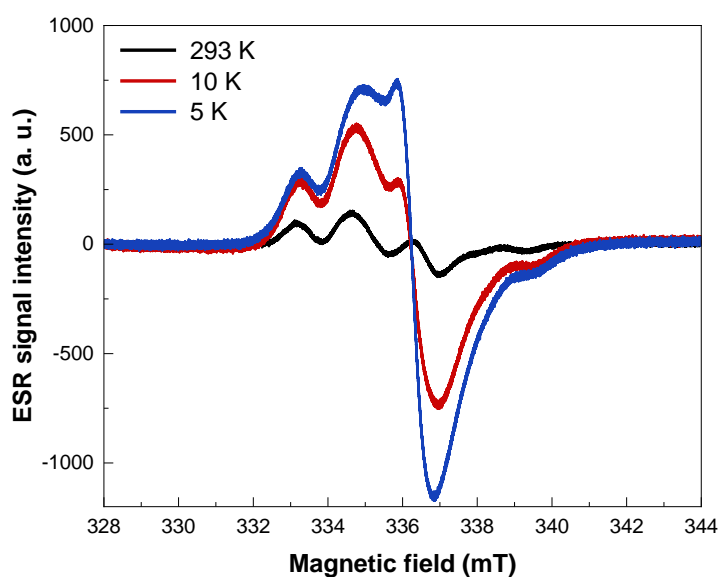


**Figure S3.** Temperature dependence of the CW EPR spectrum of UiO-66-NH<sub>2</sub>, measured at the same experimental conditions. A simultaneous increase in the intensities of the EPR peaks is observed with decreasing temperature. At 5 K in the central part of the spectrum, a single line, whose  $g$ -factor is close to 2.0023, also begins to appear.



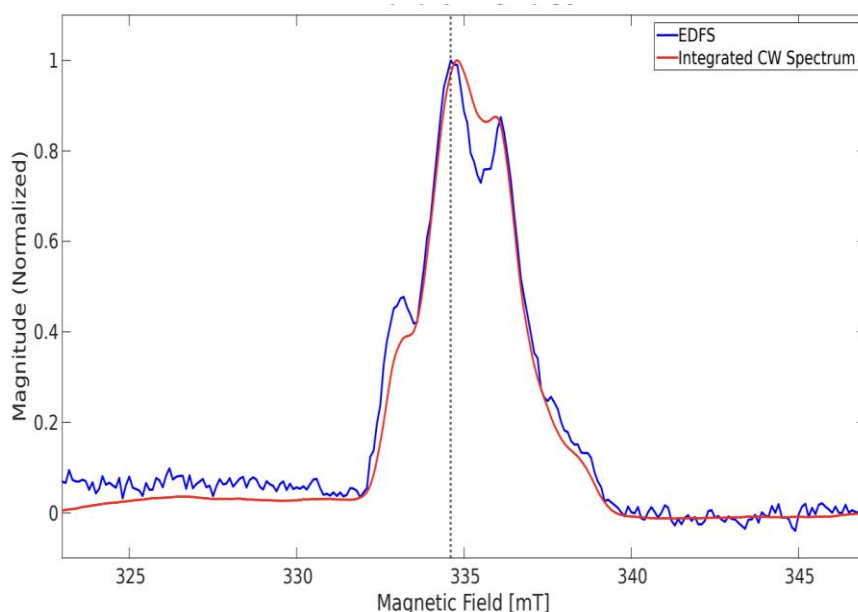


**Figure S4** X-band EDFS spectrum of the NH• spin center in UiO-66-NH<sub>2</sub> (blue) measured using the Hahn-echo microwave pulse sequence at a temperature  $T = 50$  K, shown in comparison with the integrated X-band CW EPR spectrum (red). A dotted line indicates the magnetic field used for all further pulsed EPR experiments.

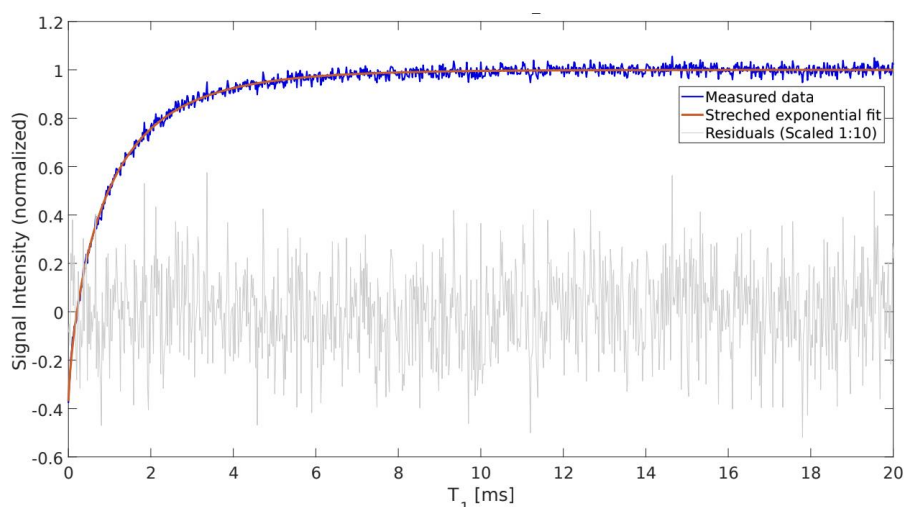


**Figure S5.** The spin-lattice relaxation time ( $T_1$ ) was determined at 50 K using the inversion recovery pulse sequence. This relaxation time reflects how quickly the spin system returns to thermal equilibrium with its lattice environment after being excited. The data were fit using a stretched exponential model, yielding a  $T_1$  of 956  $\mu$ s with a stretching parameter ( $\beta$ ) of 0.74.

## REFERENCES (SI)

1. Katz, M. J.; Brown, Z. J.; Colón, Y. J.; Siu, P. W.; Scheidt, K. A.; Snurr, R. Q.; Hupp, J. T.; Farha, O. K. A Facile Synthesis of UiO-66, UiO-67, and Their Derivatives. *Chem. Commun.* **2013**, 49 (82), 9449–9451. DOI: 10.1039/C3CC46105J.
2. Fischer, J. W. A.; Stropp, J.; Tschaggelar, R.; Oberhänsli, O.; Alaniva, N.; Inoue, M.; Mashima, K.; Barnes, A. B.; Jeschke, G.; Klose, D. Design and Performance of an Oversized-Sample 35 GHz EPR Resonator with an Elevated  $Q$  Value. *Magn. Reson.* **2024**, 5 (2), 143–152. DOI:10.5194/mr-5-143-2024.

3. Neese, F.; Wennmohs, F.; Becker, U.; Riplinger, C. The ORCA Quantum Chemistry Program Package. *J. Chem. Phys.* **2020**, *152* (22), 224108. DOI: 10.1063/5.0004608.
4. Perdew, J. P.; Burke, K.; Ernzerhof, M. Generalized Gradient Approximation Made Simple. *Phys. Rev. Lett.* **1996**, *77* (18), 3865–3868. DOI: 10.1103/PhysRevLett.77.3865.
5. Schäfer, A.; Horn, H.; Ahlrichs, R. Fully Optimized Contracted Gaussian Basis Sets for Atoms Li to Kr. *J. Chem. Phys.* **1992**, *97* (4), 2571–2577. DOI: 10.1063/1.463096.
6. Giannozzi, P.; Baroni, S.; Bonini, N.; Calandra, M.; Car, R.; Cavazzoni, C.; Ceresoli, D.; Chiarotti, G. L.; Cococcioni, M.; Dabo, I.; Dal Corso, A. QUANTUM ESPRESSO: A Modular and Open-Source Software Project for Quantum Simulations of Materials. *J. Phys. Condens. Matter* **2009**, *21* (39), 395502. DOI: 10.1088/0953-8984/21/39/395502.
7. Giannozzi, P.; Andreussi, O.; Brumme, T.; Bunau, O.; Nardelli, M. B.; Calandra, M.; Car, R.; Cavazzoni, C.; Ceresoli, D.; Cococcioni, M.; Colonna, N. Advanced Capabilities for Materials Modelling with Quantum ESPRESSO. *J. Phys. Condens. Matter* **2017**, *29* (46), 465901. DOI: 10.1088/1361-648X/aa8f79.
8. Heyd, J.; Scuseria, G.E.; Ernzerhof, M. Hybrid functionals based on a screened Coulomb potential. *J. Chem. Phys.* **2003**, *118* (18), 8207–8215. DOI: 10.1063/1.1564060.
9. Heyd, J.; Scuseria, G.E.; Ernzerhof, M. Erratum: “Hybrid functionals based on a screened Coulomb potential” [*J. Chem. Phys.* 118, 8207 (2003)]. *J. Chem. Phys.* **2003**, *124*, 219906. DOI: 10.1063/1.1564060
10. Dal Corso, A. Pseudopotentials Periodic Table: From H to Pu. *Comput. Mater. Sci.* **2014**, *95*, 337–350. DOI: 10.1016/j.commatsci.2014.07.043.
11. Stoll, S.; Schweiger, A. EasySpin, a Comprehensive Software Package for Spectral Simulation and Analysis in EPR. *J. Magn. Reson.* **2006**, *178* (1), 42–55. DOI: 10.1016/j.jmr.2005.08.013.
12. de Mello, J. C.; Wittmann, H. F.; Friend, R. H. An Improved Experimental Determination of External Photoluminescence Quantum Efficiency. *Adv. Mater.* **2004**, *9* (3), 230–232. DOI: 10.1002/adma.19970090308.